

# Chapter 7

## The AERO-VISTA Magnetometer

This chapter describes the electronics built around the HMC1053 anisotropic magnetoresistive (AMR) magnetometer [61] to create a fully featured flight instrument. This section will cover all aspects of electronics design up to the digitization of the signal. Section 8.3 will discuss how the data is stored and processed together with other instruments to form the AERO-VISTA Auxiliary Sensor Package (ASP).

### 7.1 Constraints and Interfaces

#### 7.1.1 Sensor Operational Theory

The HMC1053 magnetometer is a anisotropic magnetoresistive (AMR) magnetometer. Each axis has a balanced bridge, conceptually similar to a Wheatstone bridge [70]. The resistance of the bridge elements change with the magnitude of the incident field to produce a differential voltage. The anisotropic material changes resistance depending on the relative angle of the current flowing through the magnetic material and the magnetic field incident on the material [71]. The sensor passes currents through the four elements such that the differential voltage is a maximum for magnetic fields aligned (or anti-aligned) with the desired sensitive axis.

### 7.1.2 Sensor Interfaces

The HMC1053 magnetometer has 3 small-signal differential outputs. These outputs are proportional to the incident magnetic field in one of three axes. The polarity of the sensitivity can be inverted with the use of set/reset straps. These are coils wound around the AMR material such that a pulsed current through this circuit will realign the magnetic domains of the AMR material, changing the polarity of the signal [5]. This is useful because static instrument offsets, due either to amplification and detection circuitry, or due to the sensor itself, can be quite large (see Section 4.4.1). Inversion of the sensitive axis inverts the polarity of the desired signal but does not invert the polarity of the constant offsets, allowing for subtraction as discussed in Section 7.6. Other non-ideal effects of the magnetometer are addressed with calibration as discussed in more detail in Chapters 4 and 5.

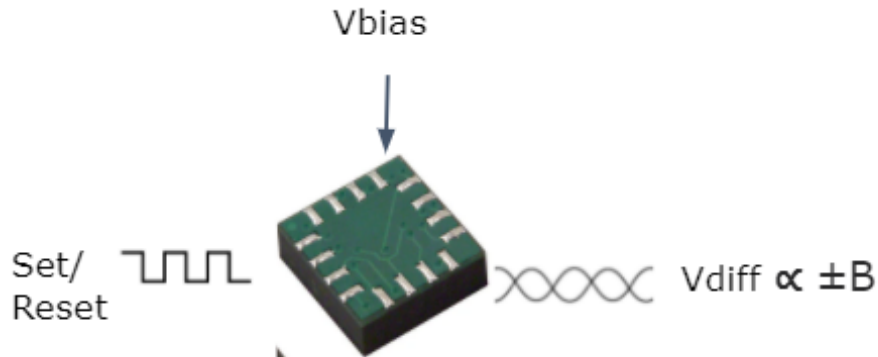


Figure 7-1: Basic operation of HMC1053 set/reset functionality. When a bias voltage is applied, a differential voltage output is proportional to the incident magnetic field. Pulsing positive or negative current through the set/reset straps inverts the output polarity.

### 7.1.3 Digitization and Storage

The magnetic data must be digitized and stored for eventual downlink to the ground for scientific analysis. In this chapter, we discuss the design of the sensor interface up to the point of digitization with an 8-channel ADC (the AD7771). Chapter 8 will discuss how this digitized signal is stored and eventually downlinked to the ground.

## 7.2 Architecture and Major Components

From Section 7.1, we need components to digitize the differential output signal and to pulse the set and reset straps. These signals are small ( $4 \mu\text{V}$  at  $100 \text{nT}$ ), and we are concerned with the noise floor, so we also pre-amplify the signal before it is digitized. The major components are diagrammed in Figure 7-2.

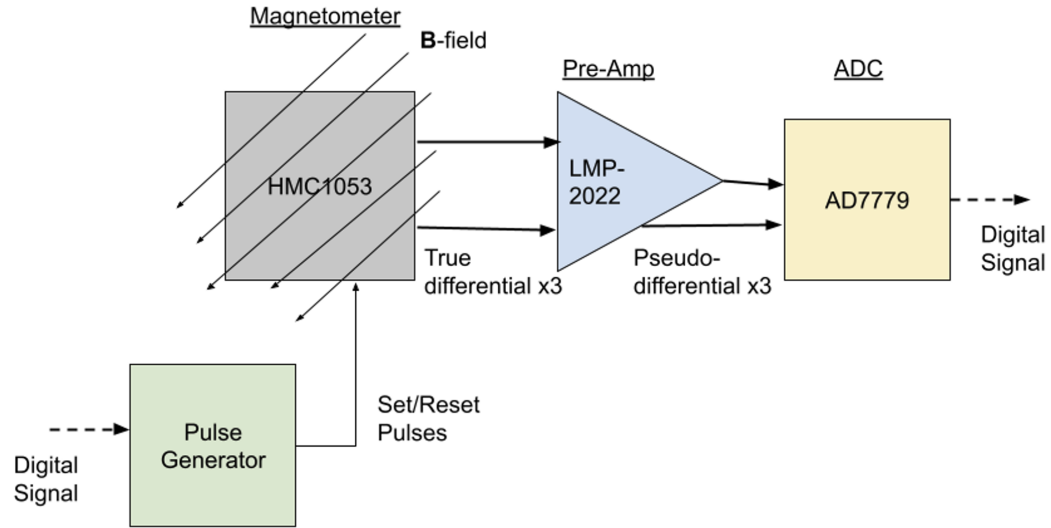


Figure 7-2: Block diagram of analog circuitry to implement magnetic sensing with the HMC1053.

### 7.2.1 Pre-Amplifier Selection

Several commercially available low noise operational amplifiers were evaluated for use in the pre-amplifier. Datasheet parameters were preferentially taken from the manufacturer's datasheet, but augmented with data from third party sources [72] where needed. Several op-amps were evaluated as listed in Table 7.4. Each op-amp was evaluated based on the following criteria:

- Added uncertainty to magnetic measurement
- Supply voltage requirement
- Power consumption
- Board space

Each parameter was quantified with a figure of merit rating from one to five, which itself was based on a value with physical units. Each figure of merit is given a weighting based on its relative importance to our use. We assigned weights of 5, 2, 2, 2 to uncertainty, supply voltage, power, and board space respectively. In the selection analysis we assumed some other characteristics of the sensing system as reported in Table 7.1. We now discuss the scoring of each parameter in detail and summarize the results in Table 7.4.

Table 7.1: Pre-amplifier selection parameterized assumptions.

<b>Parameter</b>	<b>Value</b>	<b>Reasoning</b>
Offset Calibration Period	1 second	Results in acceptable temperature drift during sample period
Maximum Temperature Drift	0.5 °C/s	Worst case thermal analysis
Bias Uncertainty Fraction	0.1	Estimate of bias which is uncalibrated
Fcutoff	100 Hz	Hardware filter frequency cutoff
Sensor Noise	95 nVrms	Magnetometer Datasheet
Supply Noise 5V	10 mVrms	Estimated from cable impedance and current draw
Other Supply Noise	0.1 mVrms	Typical LDO performance
Number Needed	8	Two magnetometers per ASP, three axes each, plus two temperature sensors
Vbias	4.096 V	Selected bias voltage for amplifiers

**Uncertainty** The amplifier contributed measurement uncertainty is the most important decision factor because precision lost at the pre-amplifier stage cannot be regained with other system modifications; uncertainty receives a weight of five. To evaluate the amplifier contributed uncertainty, we combined multiple sources of amplifier uncertainty into one input-referred nVrms value. This differential voltage uncertainty can be mapped into one nTrms value based on the magnetometer gain. In Table 7.2 we list the amplifier uncertainty contribution parameters and explain how these values map into the single input-referred differential voltage uncertainty. These calculations were implemented in a spreadsheet to calculate the results in Table 7.4.

Table 7.2: Pre-amplifier selection datasheet parameters used for uncertainty calculation. For the values used in mapping calculations, see Table 7.1.

Parameter	Explanation	Mapping to differential voltage uncertainty
$vn_{1kHz}$ (nV/ $\sqrt{Hz}$ )	Spectral voltage noise density at 1 kHz	Used with the corner frequency to calculate total voltage noise in frequency range (see Appendix E)
$en_{fc}$ (Hz)	Voltage noise corner frequency	Used with spectral noise density to calculate total voltage noise
$in_{1kHz}$ (pA/ $\sqrt{Hz}$ )	Spectral current noise density at 1 kHz	Used with the corner frequency to calculate total current noise in frequency range (see Appendix E)
$in_{fc}$ (Hz)	Current noise corner frequency	Used with spectral noise density to calculate total current noise
$Ib_{slope}$ (pA/V)	Change of input bias current with input voltage	Multiplied with sensor common mode variation and sensor source impedance
$Ib_{slope}$ (pA/C)	Change of input bias current with temperature	Multiplied with rate of temperature change and sensor source impedance
$Vos_{Drift}$ (uV/C)	Input offset drift with temperature	Scaled by expected temperature change between offset calibrations
PSRR (dB)	Power supply rejection ratio	Combined with expected supply noise estimate
CMRR (dB)	Common mode rejection ratio	Combined with bias voltage noise estimate

**Supply Voltage** The spacecraft bus can only supply the ASP with a single 5V supply. Operating from a lower voltage such as 3.3V or the 4.096V bias voltage is more desirable since these supplies can be made with low noise from a linear regulator (LDO). Operation from the 5V supply will require careful filtering and may create voltage level compatibility complications with the digital storage circuitry so is given a worse score. Operation from voltages above 5V would require a dedicated boost converter, drastically increasing design complexity and introducing new sources for noise, so no amplifiers with voltage supplies above 5V were considered.

**Power Consumption** With 16 amplifiers per spacecraft (4 per magnetometer, 2 magnetometers per ASP, 2 ASP per spacecraft), the amplifiers may contribute significantly to the power budget. We found that expected power consumption for all pre-amplifiers on one board ranged from 2.4 mW to 108 mW for the amplifiers analyzed, compared to the total ASP power budget of about 2 Watts. At less than 10% of the power budget even in the worst case, the power consumption receives a weight of two.

**Board Space** Physical space allocated to the ASPs is minimal (about  $350\text{ cm}^2$  each), so the PCBs are limited in size. Components which integrate multiple amplifiers into one package or which are available in small packages are desirable. Board layout area for the range of amplifiers considered ranged from 24 to 240 square millimeters. Even the largest size is only a few percent of the total board space available so board space receives a weight of two.

Table 7.3: Mapping of figures of merit to physical units for amplifier selection.

FOM Category	Quantification
Uncertainty	nVrms
Supply V	Voltage Supply Used
Power	mW
Board space	$\text{mm}^2$ of PCB

## Amplifier Selection Results

Table 7.4: Pre-amplifier selection trade results.

Amplifier	Uncertainty		Supply		Power		Area		Total <sup>1</sup>
	Value [nVrms]	Score [5]	Value [V]	Score [2]	Value [mW]	Score [2]	Value [mm <sup>2</sup> ]	Score [2]	
MAX9618	420	4	4.096	5	2.4	5	24	5	4.5
LT1097	382	4	4.096	5	14	3	240	2	3.6
LT1007	10,000 <sup>2</sup>	0	5	2	108	1	240	2	0.9
OPA209	767	3	5	2	88	2	64	3	2.6
LT1012	288	4	4.096	5	20	3	240	2	3.6
LT6010	217	5	4.096	5	5.2	4	60	4	4.6
LMP2022	143	5	4.096	5	44	2	60	4	4.3
OPA140	262	4	5	2	72	2	70	3	3.1
OPA2188	2502	1	4.096	5	19.2	3	60	1	2.1

<sup>1</sup> Computed with weighted average.

<sup>2</sup> Error dominated by bias current. uncertainty

From Table 7.4, we see that the part numbers MAX9618, LT6010, and LMP2022 are the most promising candidates for their high selection score. For component availability issues during supply chain disruptions of 2020 and 2021 [73], the LMP2022 was selected as the pre-amplifier over the other two most viable options.

### 7.2.2 Digital to Analog Conversion

#### Noise and Uncertainty

The analog to digital conversion itself can introduce noise and errors into the signal. The amplification of the pre-amplifier allows us to pick an ADC with less regard to the input noise voltage. We have designed a pre-amplifier with gain of about 50 V/V. Our ultimate measurement goal is 100 nT precision, so any error contribution which we can keep below about 10 nT can be largely ignored as it will likely be dominated by other error contributions. With our chosen bias voltage and pre-amplifier, a signal of 10 nT will create an ADC input voltage of about 20.5 uV.

$$V_{adc} = B * G_{mag} * G_{amp} = 10 \text{ nT} * 1 \text{ mV G}^{-1} * 50 \text{ V V}^{-1} \approx 20.5 \mu\text{V} \quad (7.1)$$

Quantization of the signal can also introduce errors. Using our 10 nT rule of thumb, we require a dynamic range of approximately 10,000, requiring an ADC with at least 14 bits. Even more bits would be preferable because this would account for static offsets that increase the total input range beyond just what's required for the magnetic measurement.

## **Sampling and Clocking**

It is also important that the ADC sample all magnetometers at once. An ADC which uses an internal MUX with a single ADC circuit will need to sample at 8 times the actual data rate to sample all channels. This aliases noise into the signal at frequencies up to 8 times the effective data rate, increasing measurement noise. This lesson was learned with the prototype board, MagEval, where the ADS1248 ADC was chosen as the measurement ADC. For MagEval testing, the ADC was run at 80 SPS to achieve an effective data rate of 10 SPS, increasing the noise of each sample. Other lessons learned from MagEval testing are discussed in Section A.2.1.

## **Component Choice**

The ADC options were also checked for added uncertainty from thermal drift of input offset and integral non-linearity, but these effects were relatively small compared to the contributions from the pre-amplifier as the signals at the input to the ADC are already amplified.

The ADC selected for the AERO-VISTA magnetometer to meet all of these requirements is the AD7771. The AD7779 was used during some initial prototyping, but component availability issues required a change of part number. These two devices have very similar analog performance, and the digital interface (register map) is identical.

## 7.3 Analog Design Implementation

With the conceptual block diagram from Figure 7-2 and with the major components selected, the next step is to implement the design in detail. This occurs in three stages. First, we fill in design details such as passive components with a full schematic capture. Next we assign physical parts to the components and layout the physical printed circuit board (PCB). Finally we have the PCB fabricated and the components populated on the board. In this section we describe schematic capture and layout of the magnetometer circuitry but leave fabrication and assembly details until Chapter 8.

### 7.3.1 Schematic Capture

The schematic for the analog design is hierarchical with the main “Magnetometers” schematic relying on multiple instances of the “Magnetometers Channel” and the “Magnetometer Filter” schematics. The magnetometer filter is the pre-ADC filter designed for a cutoff frequency of 48 Hz, and a settling time to 50 PPM accuracy of 33 ms. The filter block is used once for every ADC input (8 times per board). The magnetometer channel block is used twice per board. Each magnetometer channel independently implements the magnetometer, reference voltage, temperature sensor, set/reset switches, and pre-amplifiers for one three-axis magnetic field measurement.

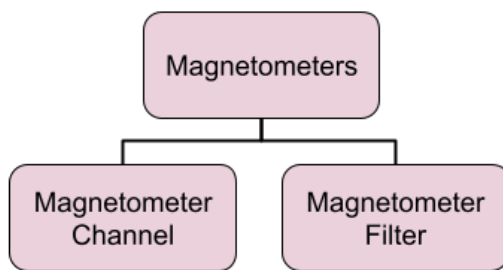


Figure 7-3: Hierarchical schematic structure for magnetometer implementation.

### 7.3.2 Layout

The magnetometers are placed as far apart as possible on the PCB while still maintaining separation from the magnetically active digital components of the Raspberry Pi and the switch mode power supplies. We minimize variation of power supply current signals in the vicinity of the magnetometers and ensure all high power current paths do not flow near the magnetometers. The magnetometers do not sit between the power supply location and any devices, so no other component current will be observed in the magnetometer measurements. The ground and power planes are left continuous under the magnetometer as the loop area with close parallel planes is smaller than that created by imbalances between current flow around the plane break if the plane was removed under the magnetometer.

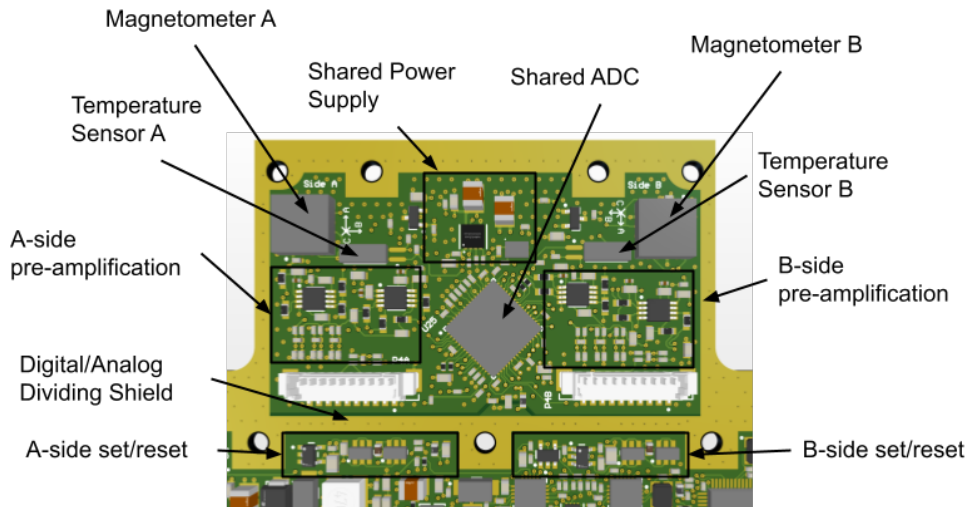


Figure 7-4: Placement for magnetometer and associated electronics. The analog signals are kept separate from the digital signals, and the magnetometers are placed as far away from metal and high current paths as possible. Figure from Hrafn V1.4.

The temperature sensor is placed as close to the magnetometer as possible to minimize temperature difference between the temperature sense location and the magnetometer location. In this layout, the edges of the two components are about 1 mm apart.

Screening of the Raspberry Pi<sup>1</sup> using techniques as described in Chapter 6 has determined that about 8 cm separation is adequate for the Raspberry Pi to be undetectable at our sensitivity threshold. The design and layout of the rest of the ASP PCB for minimization of interference with the magnetometers is discussed in Section 8.3.

## 7.4 Noise Estimation

One important contribution to the error budget discussed in Section 7.5 is the measurement noise inherent to the analog design. We analyze the magnetic design for noise contribution from the following sources:

- Magnetometer voltage noise
- Pre-amp voltage noise
- Pre-amp current noise
- Resistor noise (Johnson-Nyquist)
- ADC Noise

For each noise source, we analyze the expected spectral noise density in  $\text{nV}/\sqrt{\text{Hz}}$ . For proper comparison among all noise contributions we scale the effective noise to that at the magnetometer output based on the path gain.

**Magnetometer Noise** The magnetometer noise spectrum has been estimated from datasheet parameters as described in Section 4.4.1 and with results plotted in Figure 4-4.

**ADC voltage noise** The selected LMP2022 op-amps are chopper stabilized and have no  $1/\text{f}$  corner frequency [75]. Additionally, the input referred voltage noise density depends on the gain of the feedback network. The feedback network used in this design provides about 50 V/V gain, setting the frequency independent voltage noise contribution of the LMP2022 to  $16 \text{nV}/\sqrt{\text{Hz}}$ .

---

<sup>1</sup>Raspberry Pi Zero W version 1 [74].

**ADC current noise** The input referred noise current is mapped into voltage noise by multiplication with the impedance looking out the input terminals of the op-amp. The datasheet input-referred current noise of the LMP2022 is  $100 \text{ fA}/\sqrt{\text{Hz}}$  [75]. The sensor network differential resistance using Thevenin equivalent circuit analysis techniques is  $10.5 \text{ k}\Omega$  and is dominated by the input feedback resistors used to set a constant gain. Therefore, the equivalent magnetometer-output referred voltage noise of the op-amp current noise is given by Eq. (7.2).

$$S_V = 100 \text{ fA}/\sqrt{\text{Hz}} * 10.5 \text{ k}\Omega = 1.05 \text{ nV}/\sqrt{\text{Hz}} \quad (7.2)$$

The input resistance is adequately low such that the op-amp input current noise will not be a dominant noise source (it is always dominated by op-amp input voltage noise).

**Resistor Noise** The resistor noise is the Johnson-Nyquist thermal noise<sup>2</sup> contributed by the resistors in the analog network [72].

$$\overline{v_n^2} = 4k_B T R \quad (7.3)$$

Just as for computation with the input current noise, the Thevenin equivalent model finds a differential resistance of  $10.5 \text{ k}\Omega$ , so we can compute the rms voltage noise in Eq. (7.4).

$$\sqrt{\overline{v_n^2}} = \sqrt{(4.138 \times 10^{-23} \text{ J K}^{-1})(300 \text{ K})(10.5 \times 10^3 \Omega)} \approx 13 \text{ nV}/\sqrt{\text{Hz}} \quad (7.4)$$

This is a similar noise contribution to that of the op-amp input referred voltage noise. We have set the differential resistance to this value by design; a larger resistance will reduce the gain dependence on the variable magnetometer bridge resistance, but if it is too large it will become the dominant noise source. The differential resistance

---

<sup>2</sup>We avoid using carbon composite or thick film resistors which tend to create excess noise beyond the thermal minimum [76].

is as large as possible without turning the input resistor Johnston-Nyquist noise into the new dominant noise source.

**ADC Noise** The ADC is after the 50 V/V gain of the pre-amplifier, so all noise contributions at the input to the ADC are scaled down by a factor of 50 for comparison to the magnetometer output voltage noise. The ADC input referred voltage noise is  $270 \text{ nV}/\sqrt{\text{Hz}}$  at 1 kHz, and the integrated noise from 0.1 to 10 Hz is 6.8 uVrms. The ADC programmable gain amplifier (PGA) setting of 4V/V also provides a reduction of noise voltage rms by of about 2 as seen in plots like Figure 21 of the AD7771 datasheet [77].<sup>3</sup> These two parameters were used with a piece-wise power-law model for spectral noise density to estimate the spectral noise contribution of the amplifier as described in Appendix E.

#### 7.4.1 Results

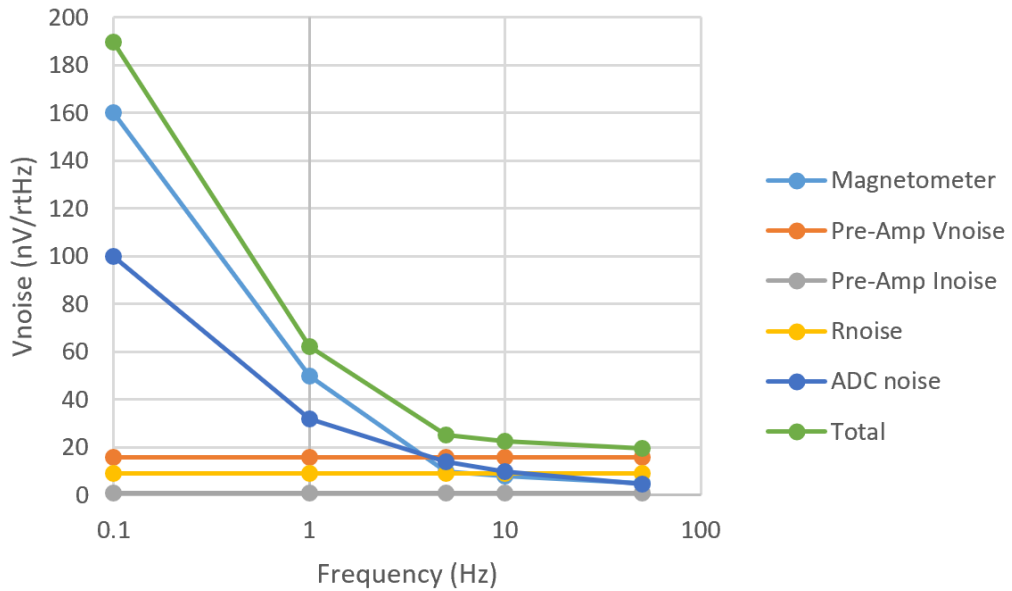


Figure 7-5: Frequency dependence of noise sources mapped to equivalent magnetometer output voltage noise.

---

<sup>3</sup>Note that on initial read, Table 25 of the datasheet [77] would seem to indicate that noise is reduced by increasing the decimation rate, and *per sample* this is true, but this does not affect the *spectral* noise density and is instead just the  $\sqrt{N}$  improvement expected with hardware averaging.

The noise contributions from each source are assumed to be independent so are summed together as the square root of the sum of squares. Individual contributions and total noise over frequency are plotted in Figure 7-5. The approximate integrated noise contribution is integrated piece-wise as described in Appendix E. Integrating from 0.1 to 10 Hz finds a total noise of 416 nVrms. This corresponds to an integrated magnetic noise of 10.1 nT. This noise value is verified by test in Section 7.7.

## 7.5 Error Budget

Table 7.5: Total magnetic sensing circuitry error budget by analysis.

	Magnetometer	Amplifier	Resistors	ADC <sup>1</sup>	Total <sup>2</sup>	B Error
<b>Offset<sup>3</sup></b>	5.12 mV	5 uV	2.9 mV	0.8 uV	5.9 mV	140 uT
<b>Offset<sup>3</sup></b> <b>Tempco</b>	2.1 uV/°C	0.02 uV/°C	0.29 uV/°C	0.04 uV/°C	2.1 uV/°C	51 nT/°C
<b>Non-linearity</b>	4.1 uV	0	0	0.03 uV	4.1 uV	100 nT
<b>Noise<sup>4</sup></b>	--	--	--	--	0.42 uVrms	10 nT
<b>Sensitivity Tempco</b>	0.29 %/°C	0	0.01 %/°C	6 ppm/°C	0.29%/°C	290 nT/°C

<sup>1</sup> ADC parameters have been scaled by pre-amplifier gain to the equivalent magnetometer output error when not defined as a fraction of full scale.

<sup>2</sup> Summed using square root of sum of squares assuming error independence.

<sup>3</sup> The offset improvement due to set/reset straps will be considered in Section 7.6.

<sup>4</sup> Noise from each source is separately considered in detail in Section 7.4. Here we just use the total noise contribution.

The error budget is reported in Table 7.5 and combines the uncertainty contribution from all sources to verify that by analysis we will meet our required 100 nT precision. The magnetometer contributions to error are dominant for all non-ideal properties except temperature coefficient of the offset. Offset effects are compensated for using the set/reset functionality of the magnetometer as described in Section 7.6.

Remaining errors due to offset, offset temperature coefficient (tempco), and sensitivity tempco will all be calibrated out as described and demonstrated in Chapters 4 and 5.

## 7.6 Sampling Method

Critical to our ability to achieve accurate magnetic measurement is the ability to calibrate out slowly varying offsets. As seen in Table 7.5, the static offset and its variation over temperature are large compared to our 100 nT measurement requirement. Here we describe how these effects can be calibrated out using the set/reset functionality of the magnetometers to periodically reverse the polarity of the magnetometer sensitivity.

Without the switching operation, we have a desired magnetic field signal  $B(t)$  and an undesired offset signal  $O(t)$ . Together these create what we actually measure:  $M(t)$ .

$$M(t) = B(t) + O(t) \quad (7.5)$$

For now we ignore the various gains and scalings that would provide physical units. The switching operation is the multiplication of another function,  $P(t)$ , so named because it comes from the polarity reversal.

$$M(t) = P(t) * B(t) + O(t) \quad (7.6)$$

We know  $P(t)$  and are measuring  $M(t)$ , but we know neither  $O(t)$  nor  $B(t)$ . With only this one equation and two unknown functions, we cannot know perfectly  $O(t)$  or  $B(t)$ ; however, by making some assumptions about  $O(t)$  we will get closer to subtracting out its effect and knowing  $B(t)$  more accurately.

Critically,  $O(t)$  does not change very quickly with time. We have seen from datasheet analysis that in the worst case the offset will change by 51 nT/°C (see Table 7.5). We have estimated that the temperature of this sensor will not change

faster than 0.5 °C/s, so the offset contribution will not be larger than 26 nT/°C. From this, we baseline a set/reset period of 1 second.<sup>4</sup>

Once we have the set/reset period, we know the function  $P(t)$  and can estimate  $B(t)$  and  $O(t)$  separately. We use the set/reset polarity change to estimate the  $O(t)$  at a regular interval; we denote this estimate as  $O'(t)$ . This in turn allows us to solve for a best estimate  $B'(t)$  which should be close to the actual  $B(t)$ .

$$M(t) = P(t) * B'(t) + O'(t) \quad (7.7)$$

$$B(t) \approx B'(t) = (M(t) - O'(t))/(P(t)) \quad (7.8)$$

Note that in this case, division by the polarity is equivalent to multiplication because  $P(t)$  is actually only ever -1 or 1. We know  $O(t)$  will change slowly with time (we've designed the set/reset period to ensure this).  $P(t) \times B'(t)$  in general does not change slowly with time, so as a first pass we can simply low-pass filter the measured signal, driving the contribution of  $P(t) \times B(t)$  towards zero and allowing us to find an  $O'(t)$ .

### 7.6.1 Frequency Domain

This switching and low-pass operation can be understood further with frequency domain analysis. A cartoon of the relevant signals in the frequency domain is shown in Figure 7-6.

The multiplication of the magnetic field signal by the polarity signal creates convolution in the frequency domain. Convolution with an impulse preserves the shape of the convolved signal. Then we can use a sharp low pass filter to find  $O'(t)$ . Of course, this is only perfect if there is no magnetic signal at the same frequency of the polarity switching (which there is). A magnetic signal at the same frequency as the polarity switching will be shifted to zero frequency, and will be included in the estimation of the offset. This is a fundamental problem which cannot be resolved

---

<sup>4</sup>This is a software-adjustable parameter so different periods may be tested in flight.

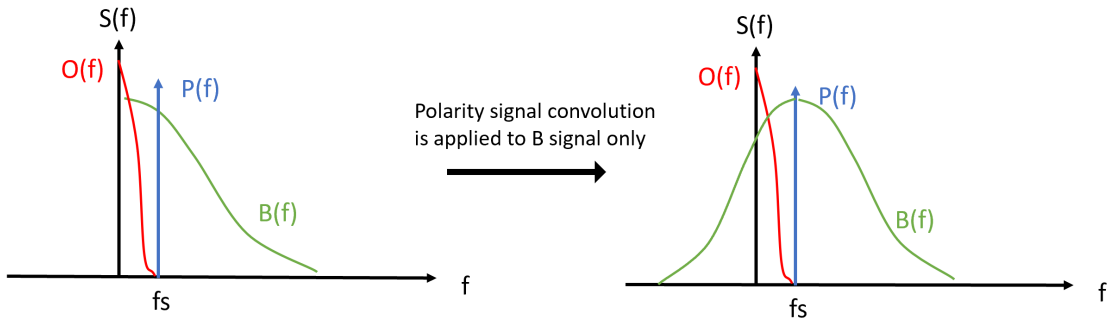


Figure 7-6: Frequency domain sketch of offset and magnetic field signals.  $O$ ,  $P$ , and  $B$  represent the offset, polarity, and magnetic field signals. Multiplication of the polarity signal in the time domain is convolution in the frequency domain. The drift of the offset occurs at lower frequencies than the set/reset rate. The polarity switching function is a square wave, so in the frequency domain is actually a sinc function, but for simplicity we've approximated it as single frequency in this cartoon.

as long as magnetic fields are changing at the same time as we are performing our switching operations. By choosing to low pass filter the measurement with the offsets included, the estimation of the offset is sensitive to magnetic changes at 1 Hz. This creates artifacts in the offset estimation that show as a strong 1 Hz square wave noise signal as seen in Figure 7-7. Looking at typical noise frequency distribution such as provided in Appendix C, this is not ideal, because noise is dense at low frequencies (like 1 Hz).

However, the density of magnetic noise decreases at higher frequencies. Additionally, the change in magnetic signal due to reorientation of the spacecraft will be of the same frequency as the rotation rate of the spacecraft, very low, on the order of mHz. Therefore, the best estimate of the offset is achieved by minimizing the amount of time between the measurements used to estimate the offset.

The settling time of the analog hardware sets a minimum amount of time between the last positive polarity measurement and the first negative polarity measurement on either side of a switching event. As implemented, this settling time is 33 ms for 50 ppm settling accuracy. Rounding up, this requires ignoring 2 samples (40 ms). Instead of sampling the offset with a square wave, we now have the sampling waveform shown in cartoon in Figure 7-8. We call this “boundary sampling” because

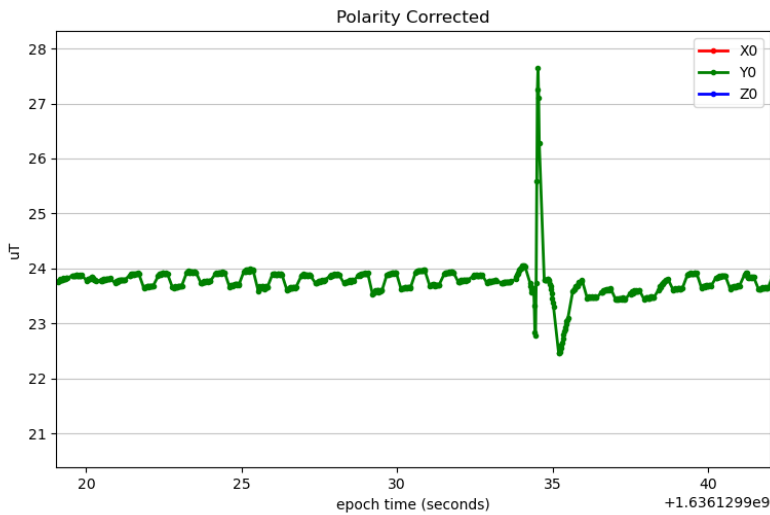


Figure 7-7: 1 Hz artifacts from poor estimation of offset in the presence of magnetic noise signals.

instead of sampling the offset with all of each set/reset state, we are only sampling on the boundaries of the polarity switching events.

We implement this waveform in a MATLAB simulation as shown in Figure 7-9. With this implementation, we can compute the spectral power density of the sampling (estimated with the MATLAB periodogram function<sup>5</sup>) as in Figure 7-10. The boundary sampling method captures less low-frequency content, and therefore the offset estimation will be less affected by magnetic signal change which is more powerful at low frequencies.

---

<sup>5</sup>see <https://www.mathworks.com/help/signal/ref/periodogram.html#d123e121332>

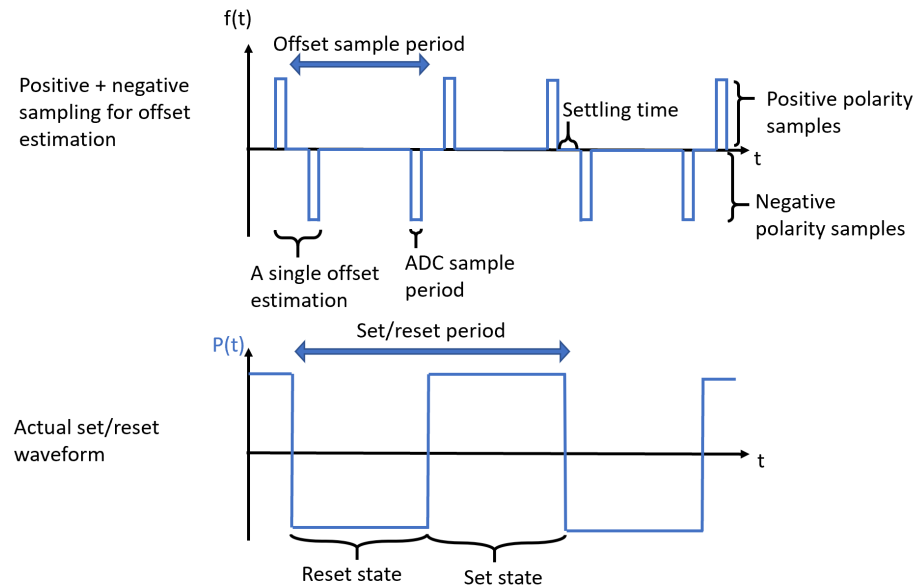


Figure 7-8: Cartoon of the boundary sampling method with major features indicated. The closely spaced positive and negative samples reduce the amount of low frequency magnetic signal included in the offset estimation.

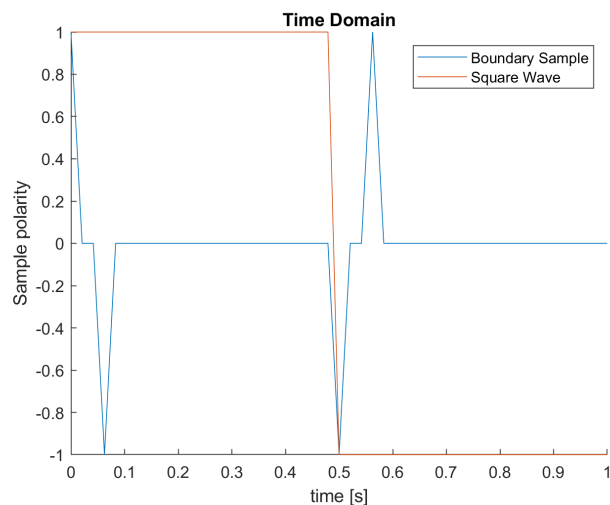


Figure 7-9: Implementation of the boundary square wave sampling waveforms in MATLAB. The periodogram of these waveforms are shown in Figure 7-10.

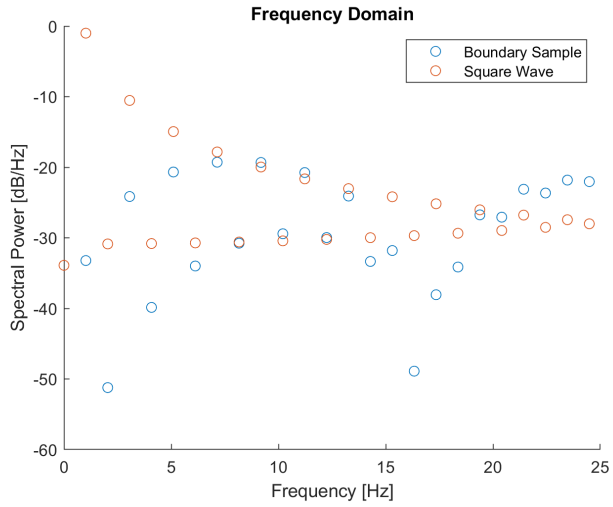


Figure 7-10: Power spectrum of the boundary sampling and square wave sampling methods computed by periodogram of the signals in Figure 7-9. The boundary sampling method captures less power than the square wave at low frequencies.

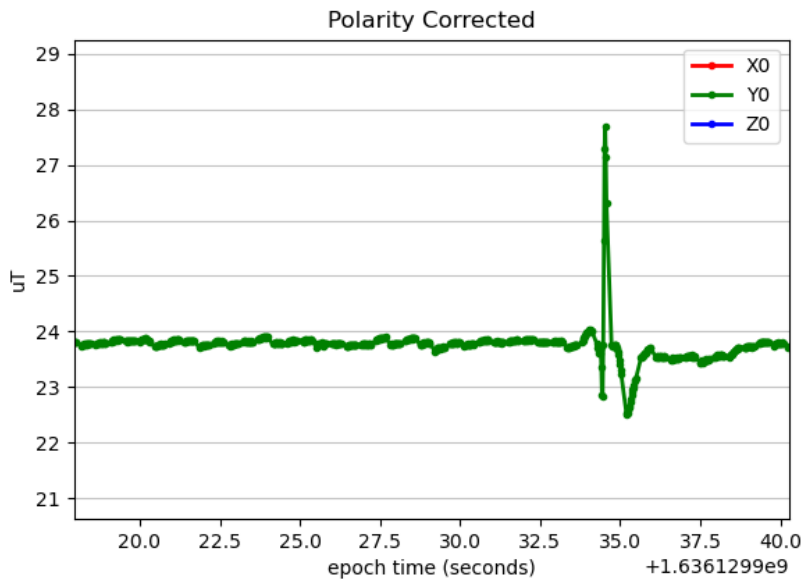


Figure 7-11: Minimum period estimation of offset has removed the 1 Hz artifacts seen with 1 Hz square wave offset sampling in Figure 7-7.

## 7.7 Engineering Model Measurement Results

The magnetic measurement circuit described in this chapter is implemented in a stand-alone payload (the ASP) described in Chapter 8. We evaluate the as-built noise floor performance in a mu-metal shielded room, similar to the test described in Section 4.4.2.

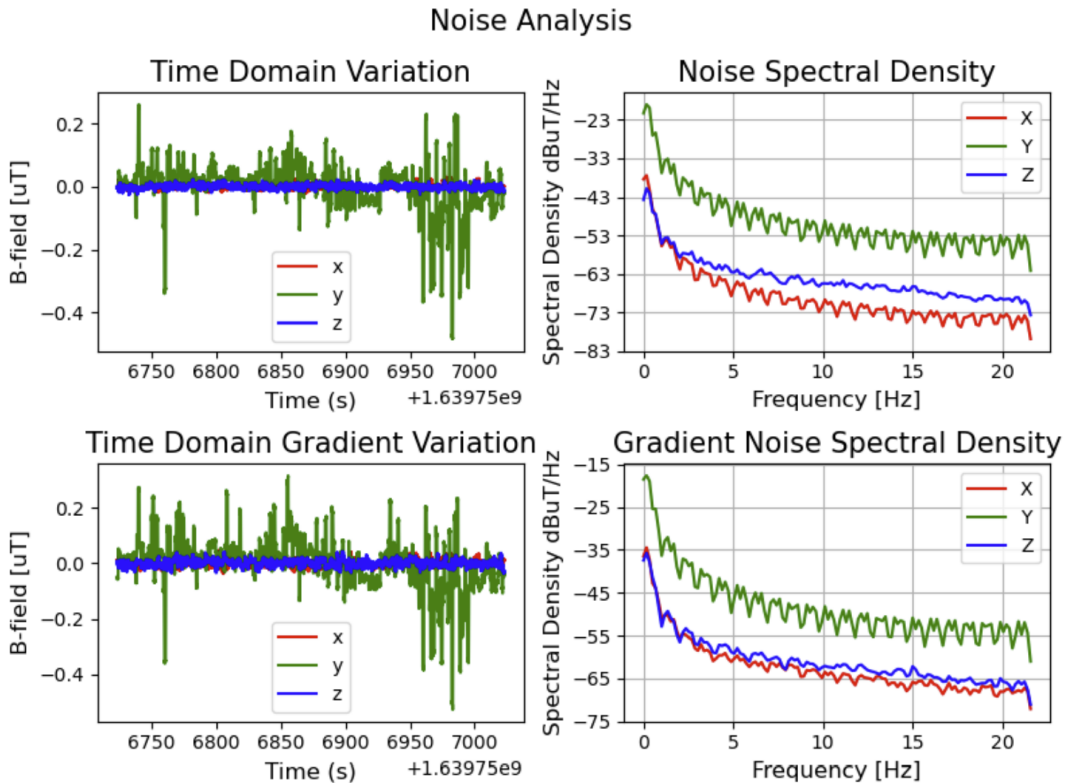


Figure 7-12: Measured noise of the engineering model. Left figures show the time domain magnetic field measurements and the right figures show the frequency domain. The top figures plot the magnetic field of magnetometer A, and the bottom plots the difference between magnetometers A and B. The Y-axis noise is significantly higher but still meets 100 nTrms measurement requirements. The effect of the 1 Hz set/reset switching is seen with its harmonics in the spectral density plots.

From 0.1 to 10 Hz, the expected noise by analysis was about 10 nTrms. The measured noise in nTrms for the 3-axes was [9.3, 87., 7.1]. The X- and Z-axes seem to verify our analysis in the noise budget. The larger Y-axis noise is likely due to self-interference from the Raspberry Pi computer (Y-axis is normal to the plane of

the Raspberry Pi PCB), though may be due to other switching electronics in the ASP PCB. The Y-axis noise is higher in both magnetometers, though is slightly lower at 45 nTrms in magnetometer B. Despite the worse performance in the Y-axis, we are meeting the 100 nT requirement in all axes.

## 7.8 Summary

This chapter has covered the electronics design around the HMC1053 magnetometer. This device produces a small differential output proportional to the incident field. This small signal is amplified by an op-amp pre-amplifier, and then digitized by a simultaneously sampling analog to digital converter. We discussed the implementation of the analog signal chain including schematic capture and PCB layout. The PCB was designed to minimize the magnetic interference from other components on the magnetometers. This design's total analog signal noise was estimated for all sources and combined to produce Figure 7-5. The noise estimate was combined with other error sources to create a complete error budget in Table 7.5.

Offset effects create very large error, but the static and slow-varying offsets can be estimated by flipping the sensitive polarity of the AMR magnetometer. By sampling the output with both a positive and negative sensitivity we can estimate which part of the signal was caused by the magnetic field and which was caused by the instrument offset. This sampling will always partially combine the magnetic field and offset signals, but by acknowledging that the offset changes very slowly, we are able to separate the two effects in the frequency domain. We identified an improved offset sampling method which minimizes the amount of magnetic signal contribution to the offset estimate.

The design described in this chapter has been shown to meet AERO-VISTA's measurement requirement of 100 nT precision with repeatability over spacecraft operating conditions. Chapter 5 reports performance of the implemented magnetometer when combined with our calibration method. In Chapter 8 we describe how this magnetic

sensing circuitry and PCB layout has been implemented on a stand-alone payload, the Auxiliary Sensor Package (ASP).

This page is intentionally left blank.

# Chapter 8

## The AERO-VISTA Auxiliary Sensor Package Design

### 8.1 ASP Introduction

The AERO-VISTA magnetometers are implemented on a payload called the Auxiliary Sensor Package (ASP). This payload is independent from the main Vector Sensor payload which performs RF processing and storage (see Section 1.1.3). The ASP provides data which contextualizes the data captured by the main science instrument. This includes observations to localize radio emissions observed by the vector sensor with respect to Red and Green line auroral arcs [78]. The ASP can also observe the shape and deployment status of the vector sensor antenna elements. Finally, the ASP measures the local magnetic field to determine the direction of RF-wave propagation with respect to the local magnetic environment. The magnetometer data can also be used to observe the presence of field aligned currents which perturb the local magnetic field away from what would be predicted by a global magnetic model.

To meet these requirements, the ASP incorporates two types of instruments: a RGB camera and magnetometers. The camera is used to observe auroral emissions and to image the deployed antenna. The magnetometer on the ASP meets the magnetic science sensing requirements for aligning the RF waves with the local magnetic field.

The main components of the ASP are:

- **Computer:** A Raspberry Pi Zero is a small and low power single board computer with significant community support and software packages readily available [74]. All software on the ASP is implemented on the Raspberry Pi Zero.
- **Magnetometers:** Two Honeywell HMC1053 magnetometers provide a spatially diverse measurement of the in-situ magnetic field amplitude and vector direction measurements. A custom analog system is built around these magnetometers and described in detail in Chapter 7.
- **Engineering Camera:** A Raspberry Pi Camera (V2.1) [79] provides optical measurement of auroral events and confirmation of antenna deployment. This camera is designed for use with the Raspberry Pi computer and no custom electronics are required for connection.
- **Custom PCB:** A custom PCB integrates the analog electronics for the magnetometers, power distribution electronics, and digital interface electronics for the ASP. The design of this PCB is described in detail in Section 8.3.
- **Custom Aluminum Enclosure:** The aluminum enclosure provides mechanical support to the other elements of the ASP, and also serves as an EMI shield between the ASP components and the vector sensor. The enclosure is described in detail in Section 8.4
- **Cables and GSE:** The cables connect the ASP to the spacecraft bus and vector sensor to provide necessary power, clock, and data connections. Ground support equipment (GSE) is used for ground testing of the ASP.

The ASP functional diagram in Figure 8.1 describes the interfaces internal and external to a single ASP module. There are two ASP modules per spacecraft, and then two spacecrafts (AERO and VISTA) for a total of four in-flight ASPs. The Raspberry Pi plugs into the PCB such that the PCB can be considered an unusual form factor and very customized “hat” for the Raspberry Pi [80]. The ECam is separate from the PCB, but is still internal to the ASP module. The ASP receives power and a data

connection from the spacecraft bus (called the M6P bus), and receives a synchronized clock signal from the vector sensor payload.

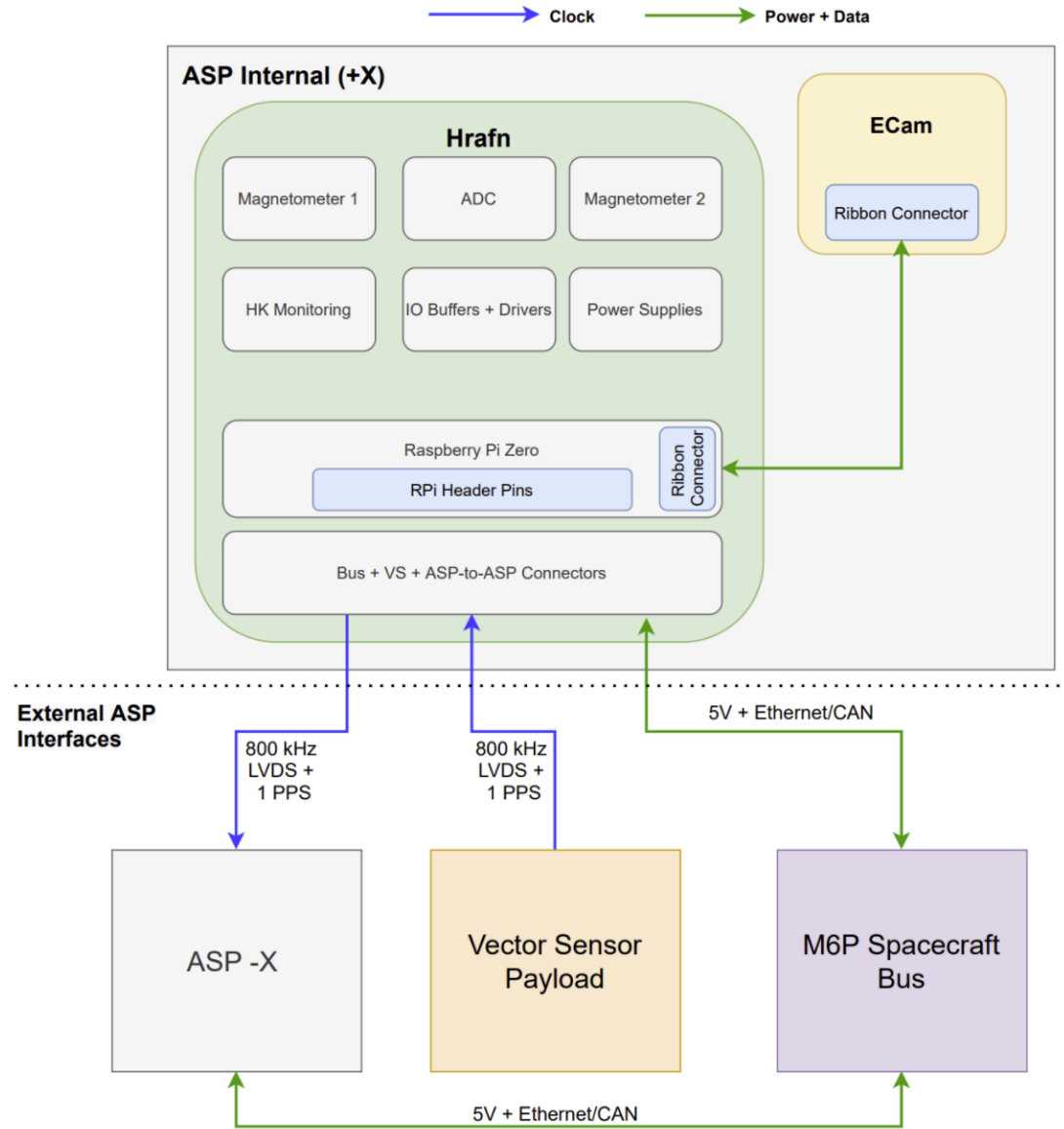


Figure 8-1: ASP Functional Diagram. Functionality that resides on the custom PCB is shown in the green box. Connections from the PCB to other devices show interactions with other ASP system components.

## 8.2 Imaging System

The ASP can take pictures or videos with a Raspberry Pi Camera V2.1. Software configuration of the camera over command allows us to set the integration time of each image to between 0.1 and 10 seconds. A 195 degree field of view fisheye lens is used with the Pi camera to image one hemisphere of the vector sensor antennas. With two ASP modules on each spacecraft, the two cameras together can image the entire vector sensor. See the thesis by Cadence Payne for more details on optical sensing with the ASP modules [78].

## 8.3 Electronics Design

The ASP electronics are implemented on a custom PCB. This PCB is formally known as the “ASP PCB”, but has been given the additional informal name “Hrafn” which shows up in project documents.<sup>1</sup> The electronics are designed to support the hardware which meets mission requirements, primarily the Raspberry Pi, the magnetometers, and the Pi Camera. Key functions include providing power to the sensors and the computer, creating a data connection between the ASP computer and the spacecraft bus, providing overcurrent fault protection for tolerance to radiation effects like latchup, and monitoring the general health and status of the instruments. Additionally, the electronics have been designed to produce low EMI, particularly any EMI which might not be phase locked to the vector sensors ADCs, and has been designed for quick and inexpensive development.

The major functionality of the Hrafn PCB is diagrammed in Figure 8-2, including the part number selection for major components. The digital interfaces were tested with evaluation modules in a breadboard format and stand alone Raspberry Pi (using

---

<sup>1</sup>The name Hrafn follows a spacecraft-wide theme of naming PCBs in various Scandinavian languages. This theme was adopted since the spacecraft will be observing Earth’s Aurora which are famously visible from high latitudes. The name Hrafn is the Old Norse word for raven, a reference to the two ravens Huginn and Muninn who roosted on Odin’s shoulder. The two would fly all over the world to report their observations back to Odin [81]. With two ASPs in the “shoulder” of each spacecraft, each taking pictures, the ASPs are the Huginn and Muninn to the Odin of the rest of the spacecraft.

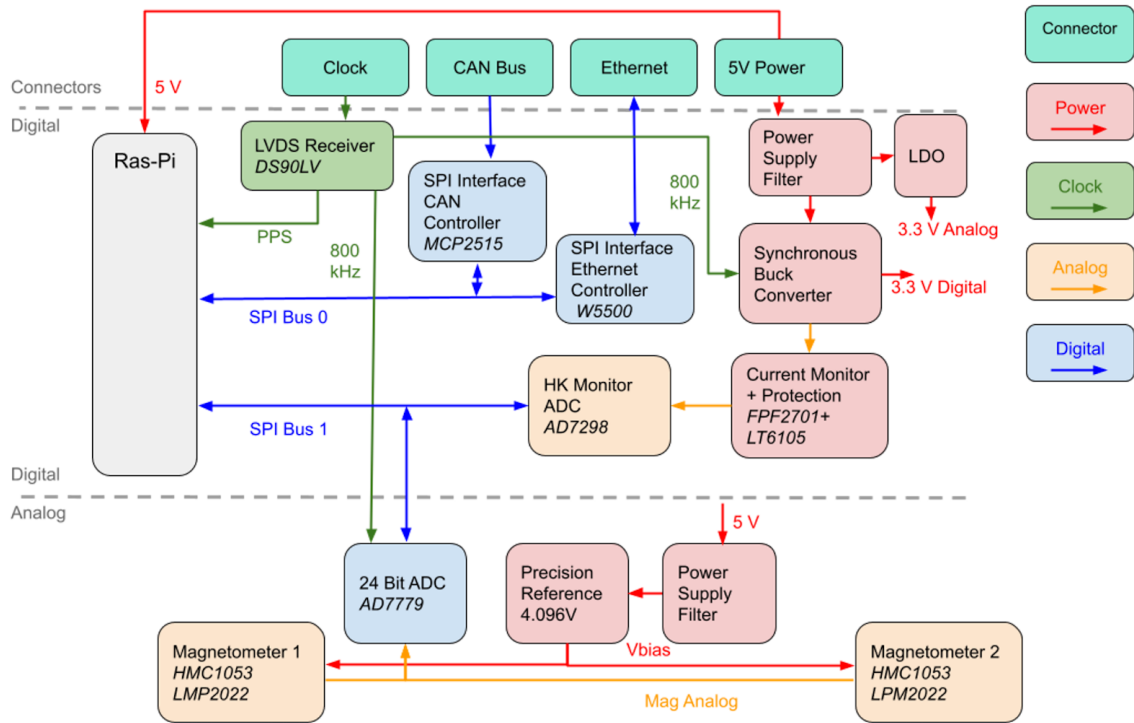


Figure 8-2: ASP PCB functionality block diagram with part numbers for major components indicated in *italics*.

a prototype called the ASPIT, see Section A.2.3). The magnetometer design was tested with the magEval implementation of the HMC1053 magnetometers (see Section A.2.1). The ADC interface was tested with a custom AD777x evaluation board (see Section A.2.2). These devices together allowed us to incrementally write software, debug, and refine our design before committing to the final version with the Hrafn PCB.

### 8.3.1 Schematic Capture

Following block diagram creation and testing with prototypes and evaluation modules, a detailed schematic was captured with Altium designer. We organized the schematic design with a hierarchical format as summarized in Figure 8-3. A top level schematic implements the connections between the different sub elements and an annotated screen capture of the top level schematic is shown in Figure 8-4.

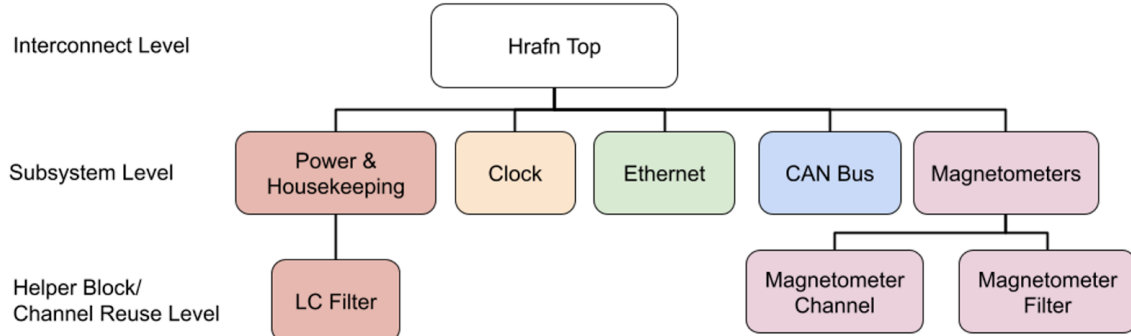


Figure 8-3: ASP PCB hierarchical design for schematic capture.

## Power Supplies and Housekeeping

The power supply and housekeeping section provides power to the devices on Hrafn including the Raspberry Pi. Ultimately all power in the ASP comes from a 5V supply from the spacecraft bus electrical power system (EPS).

## Clock

The clock section of the PCB includes the ability to receive, resend and detect LVDS clock signals. We have included the ability to switch from the external clock to an internal clock generated by the Raspberry Pi to allow the magnetometer ADC to operate even when the ASP is disconnected from the spacecraft (such as during bring-up testing) or when the ASP is operating but the vector sensor is turned off (such as during the acquisition of magnetometer calibration data).

The 800 kHz clock signal from the Vector Sensor is phase synchronized with the 50 MHz reference clock used to discipline the RF ADCs. The ASP uses the 800 kHz clock to discipline the switch mode power supplies (SMPS) to keep EMI emission phase locked to the ADC sampling, making it easier to filter. Additionally, the 800 kHz clock is used to discipline the magnetometer ADC so those samples are also phase locked to both the EMI emission of the spacecraft and to the RF sampling of the main vector sensor payload.

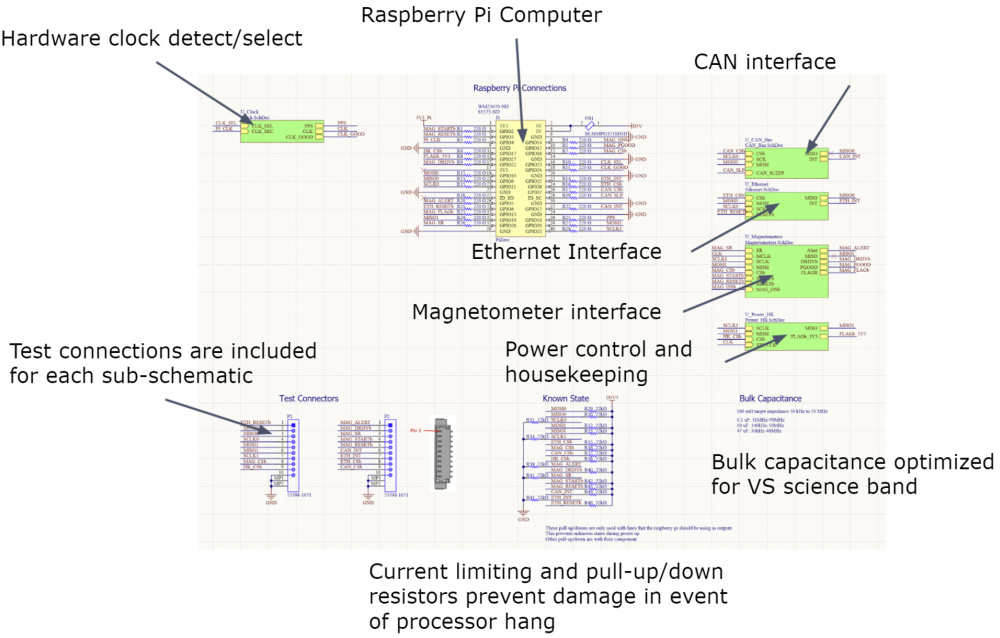


Figure 8-4: ASP PCB annotated top-level schematic. Filename: Hrafn\_Top.SchDoc Version: 1.4.

## Ethernet and CAN Interfaces

The Ethernet and CAN capabilities are provided by SPI interfaced network controllers, the MCP2515 for CAN capability, and the Wiznet W5500 for Ethernet. Both of these devices have device tree overlays already built into Raspbian as discussed in Section 8.5.3.

### 8.3.2 Layout and PCB Design

#### Placement

Layout of the Hrafn PCB first required the creation of a floor plan with rough placement goals for each major subsystem. It was at this point that EMI and magnetic interference considerations were used to keep switching or other magnetic components as far away from the magnetometers as possible. The floor plan was then used to create an initial placement of all components as shown in Figure 8-8.

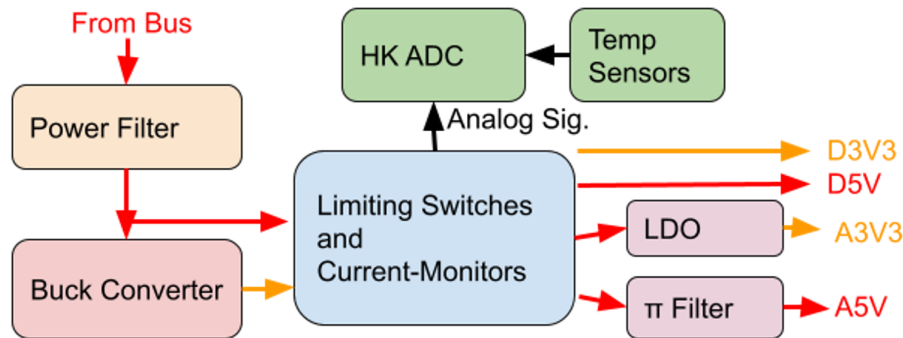


Figure 8-5: ASP PCB Power Supply and Housekeeping Section Block Diagram

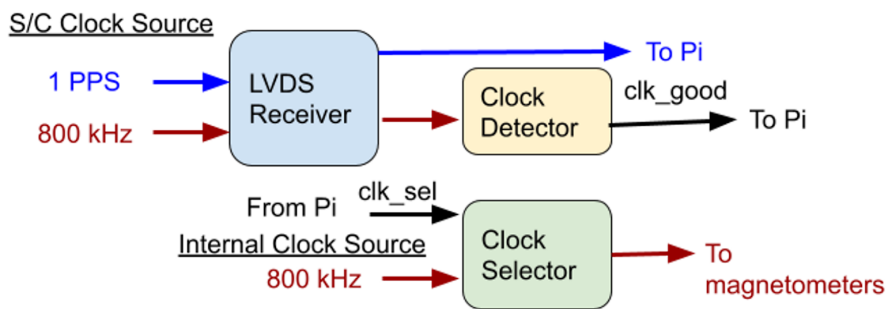


Figure 8-6: ASP PCB clock section block diagram.

Primary drivers during floor plan design include:

- Proximity of highly interconnected subsystems to keep total routing lengths short.
- Distance between the Ethernet magnetics to the magnetometers.
- Distance between the Raspberry Pi and the magnetometers.
- Distance between the switch mode power supply and the magnetometers.
- Distance between the two magnetometers (for spatial diversity of measurement).
- Placement of the magnetometer temperature sensors as close to the magnetometers as possible.
- Minimization of total current path lengths for the power supplies.

## Stackup

The Hrafn PCB is designed with eight copper layers. EMI shielding is provided by two unbroken ground planes (except at digital/analog interface) on layers 2 and 7,

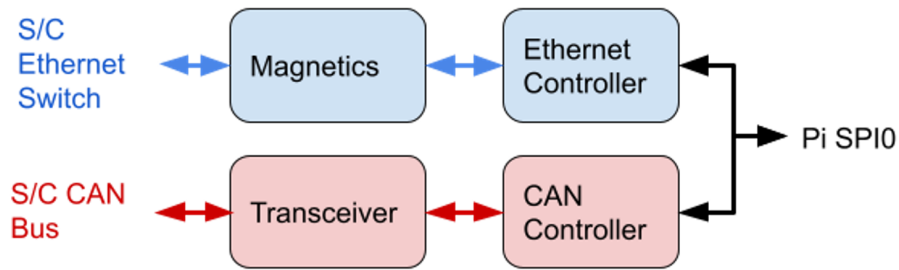


Figure 8-7: ASP PCB data interface section block diagram.

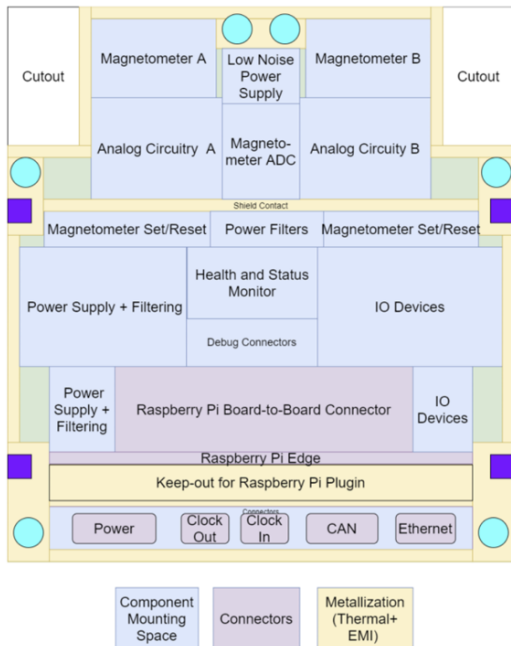


Figure 8-8: Hrafn initial floorplan.

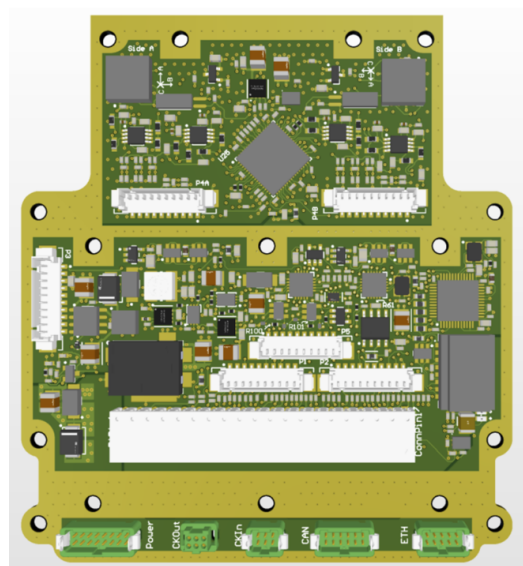


Figure 8-9: Hrafn layout in 3D rendering.

one layer into each side of the board. The outermost layers are used for components and low speed routing only as the short traces associated with component teardrops or low switching speed will keep EMI down. This is important as these layers do not have PCB shielding for EMI reduction. The innermost layers are used for the power planes, where generally one plane is used for 3.3V and the other for 5V. The two layers between a ground plane and a power plane are used for the long and/or high-speed routes. The placement of these signals between the two reference planes provides a relatively constant impedance (except for at plane boundaries) and the presence of both top and bottom ground planes in the stackup will minimize EMI

leakage from these signals.

## Analog and Digital Domains

The analog and digital domains on the Hrafn PCB are separated for reduced coupling of digital noise onto the analog electronics. Both the ground and power planes are split and a single connection is made across the divide. Details of the power supply connection of the ground and power planes between the analog and digital sections are shown in Figure 8-10.

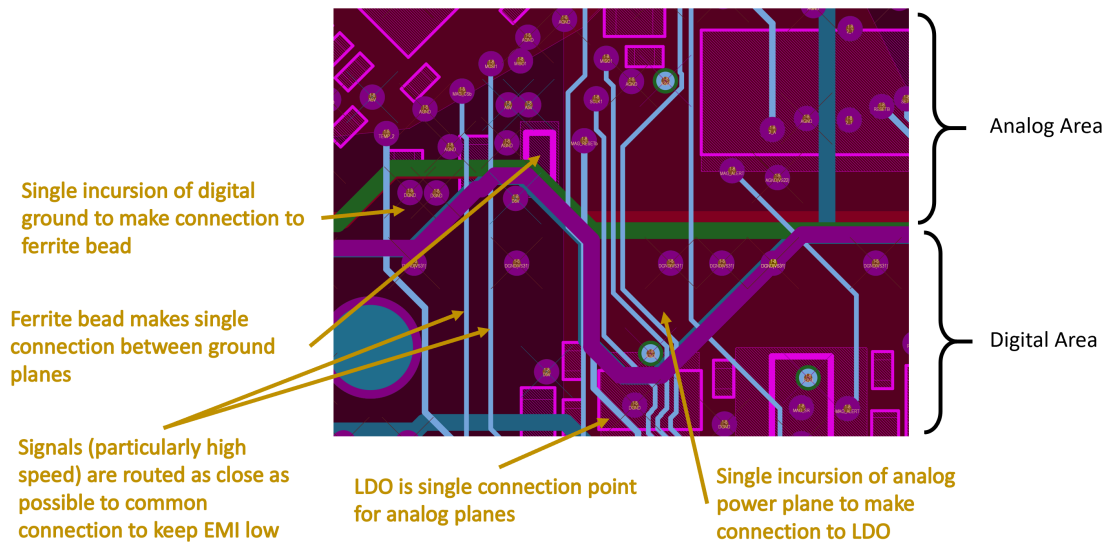


Figure 8-10: Connecting the digital Section to the analog section.

## Magnetometer Area Layout

It is particularly important that layout around the magnetometer keep time-varying magnetic fields to a minimum. Magnetic fields fall quickly with distance (see Chapter 2), so the area immediately around the magnetometer is of critical importance. To achieve this, no traces are routed underneath the magnetometer, except the differential outputs whose currents are proportional to the magnetic signal. The current flowing through these traces is on the order of microamps and any perturbation caused

by these currents will be linear with magnetic field and therefore can be calibrated out together with the instrument sensitivity matrix (see Chapter 5).

The largest current which flows near the magnetometers is the bias current for the magnetometer itself. This current is static as long as the bias voltage and magnetometer sensor bridge resistances are static. The bias voltage comes from a precision shunt regulator with a 50 ppm/ $^{\circ}\text{C}$  drift with temperature. Any change in resistance of the coils will also correspond to a temperature or ambient field effect and therefore should be calibrated out with the temperature dependence of the offset vector. To minimize the uncertainty of any non-linearity in the change in current used to bias the magnetometer, the ground and power planes are continuous underneath the magnetometer. While current may flow underneath the magnetometer, the distance invariance of magnetic fields created by large sheets of current causes the supply and return current paths to cancel. In contrast, if the planes are removed underneath the magnetometer, any imbalance in resistance on either side of the break will cause an effective current loop generating a relatively large magnetic field. Additionally, vias which bring the bias current into and out of the magnetometer are kept close to the magnetometer chip and are outside the footprint of the magnetometer (not under it) to keep distances from any possible magnetic source at a maximum. The power supply plane is split near the magnetometers so that the magnetometer bias voltage current can occupy an entire plane and so any power supply noise on the larger analog power supply plane is isolated from the magnetometers.

Other components are kept as far away from the magnetometer as possible. The closest other component is the temperature sensor which has microamp level current which is definitionally proportional to temperature. The next closest components are the small signal pre-amplifiers whose bias currents are on the order of microamps.

## 8.4 Mechanical Design<sup>2</sup>

The ASP is a standalone payload in its own aluminum enclosure. The enclosure provides mechanical support for the electronic components including the Hrafn and camera, and it also creates EMI shielding between the ASP electronics and the vector sensor payload.<sup>3</sup> The enclosure also provides for thermal dissipation from components within the ASP and secondarily creates an EMI shield between the digital and analog sections of Hrafn.

The external interfaces to the ASP enclosure are driven by the bus interface requirements. A CAD rendering with bus interface locations marked is provided in Figure 8-11.

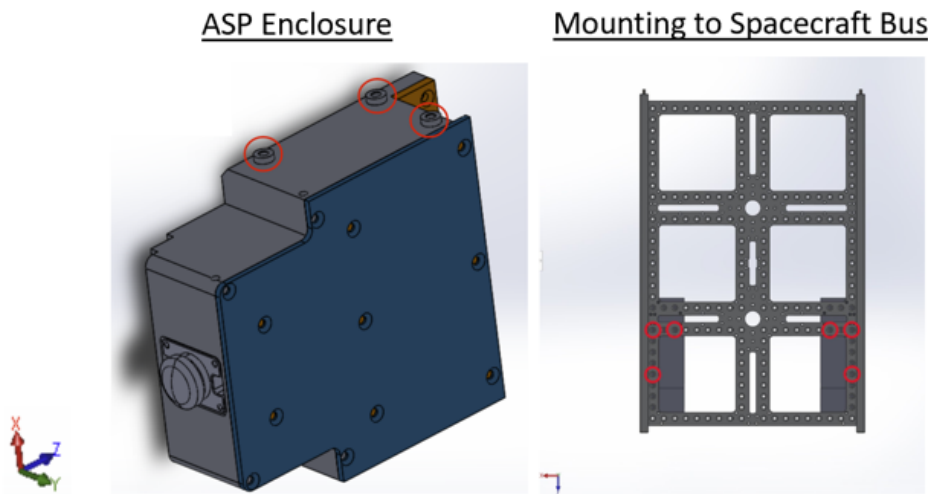


Figure 8-11: ASP enclosure mounting. Interfaces between the ASP enclosure and the mechanical bus are indicated with red circles in both pictures.

The main box of the enclosure is referred to as the “tub” and contains ledges which contact the Hrafn PCB metallization areas for mechanical support, thermal contact, and EMI sealing. An annotated CAD rendering of the ASP tub is provided in Figure

---

<sup>2</sup>The mechanical design was not primarily performed by the author of this thesis and is only briefly included here for completeness. I thank Cadence Payne for leading the design of the aluminum enclosure, and Dylan Goff and Cici Mao for valuable contributions as undergraduate researchers.

<sup>3</sup>This shielding is particularly important because the switch mode power supply on the Raspberry Pi is the only SMPS in the spacecraft *not* synchronized to the 800 kHz signal which is phased locked to the RF ADCs.

8-12.

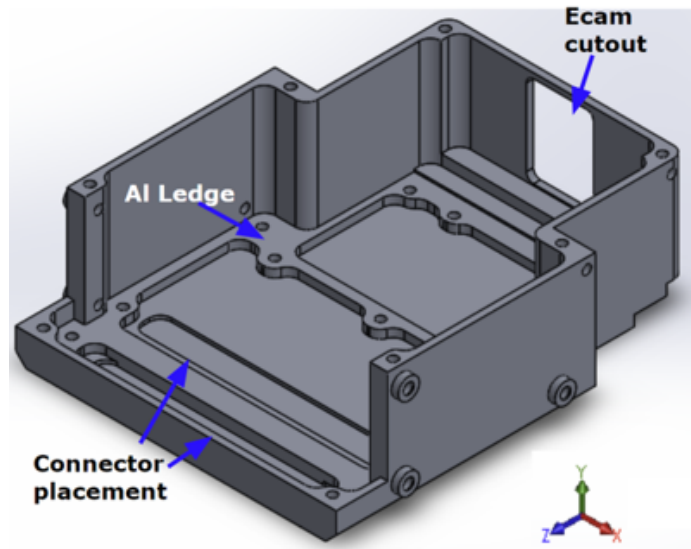


Figure 8-12: ASP enclosure tub. The aluminum ledge provides EMI sealing and thermal connection by contacting the metallization areas of the Hrafn PCB. The deeper cutouts in the tub provide spacing for the through-hole connector pins.

The tub also includes mounting points for aluminum shields which ensure that no EMI can leak out of the ASP enclosure and that minimal EMI can leak from the digital section of the Hrafn to the analog section. An annotated side view of the ASP enclosure to show placement of shields is provided in Figure 8-13.

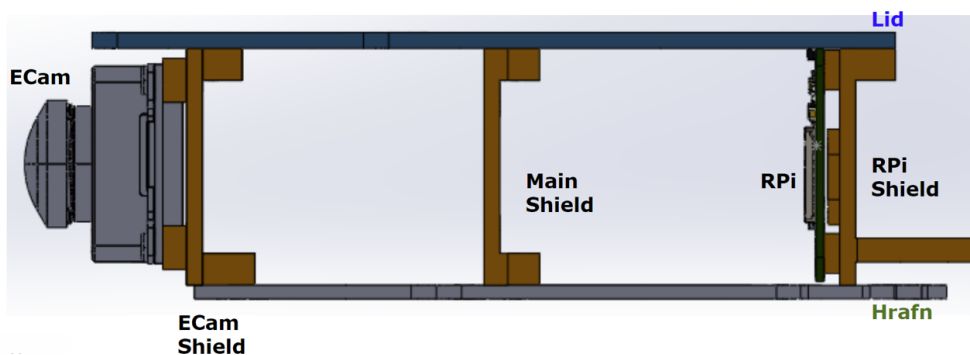


Figure 8-13: ASP enclosure shields.

## 8.5 Software Design<sup>4</sup>

### 8.5.1 Command and Telemetry Dictionary

The software system bridges the gap between functional hardware and satellite operations. With the Hrafn PCB manufactured and tested, we have hardware which is proven to be able to meet the requirements (such as described for magnetic sensing in Section 4.2). However, there is an additional level of abstraction needed before we can begin to operate the ASP payload as a “user”.

We have formalized this abstraction by writing a command and telemetry dictionary which defines every activity which we might request the ASP to perform and defines every bit of data we can bring back from the ASP. After hardware bring-up testing, we already have drivers or application programming interfaces (APIs) for the major components on the Hrafn. Therefore, the remaining software design connects each command and telemetry value to the correct hardware subsystem and associated API.

### 8.5.2 Software Block Diagram

The desired software functionality is broken up into major functions which interact with each other through limited interfaces. The abstraction represented in Figure 8-14 is used to identify separate modules, which became separate files (or a set of separate files). In the language of Python development, many of the modules are a Python class implementing an abstraction of their underlying hardware. Every activity in the command dictionary maps to one of the functions in the module class. Therefore, the main software loop only needs to parse the incoming command, and call the appropriate class function in the correct module. Many of the activities which might be called from the main loop take several minutes to complete (such as a 500

---

<sup>4</sup>The author wrote much of the low-level drivers for hardware like the ADCs. The author recognizes undergraduate researcher Luc Cot for writing file management and command processing software and the author thanks Dr. Alvar Saenz-Otero for assistance with the CubeSat Space Protocol and general software development mentoring. The software discussion here will be kept short and is intended only to provide context for the rest of the ASP payload design.

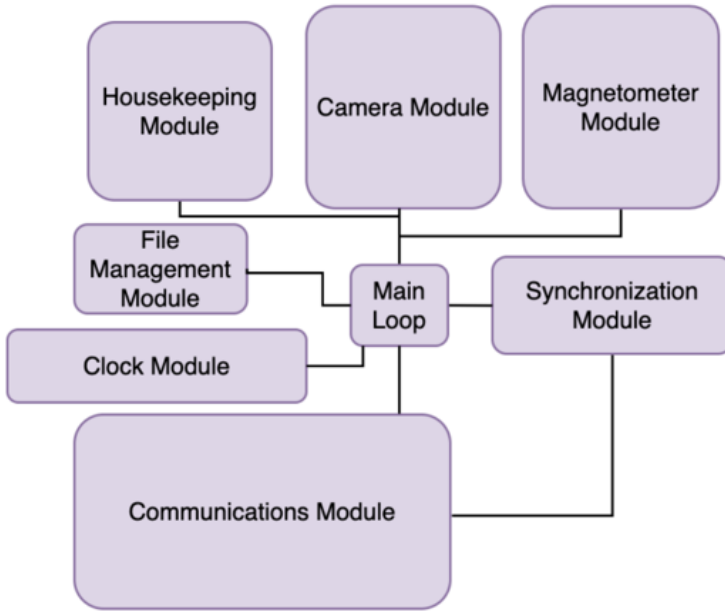


Figure 8-14: Software block diagram.

second collection sequence of magnetometer data), so the module function spins off a separate thread to complete the task, allowing the main software loop to process other commands and perform other activities.

### 8.5.3 Linux Configuration

The software is developed on the Raspberry Pi Zero in the Raspbian operating system.<sup>5</sup> Device trees which come with Raspbian are available for the W5500 Ethernet controller and the MCP2515 CAN controller. The devices are enabled by editing the `/boot/config.txt` file to include the overlays.<sup>6</sup> We have also enabled the second SPI bus with two chip select lines for use with the magnetometer ADC and the housekeeping ADC.

---

<sup>5</sup>We have frozen development with Raspbian Buster with Linux kernel V4.19. At the time of writing, this is available at: <https://downloads.raspberrypi.org/raspbian/images/raspbian-2019-07-12/>.

<sup>6</sup>A helpful list of Raspbian overlays with definitions of optional parameters is provided at the following link: <https://raw.githubusercontent.com/raspberrypi/firmware/master/boot/overlays/README>.

## 8.6 Summary

This chapter covered the payload design surrounding the magnetic sensing system. The Auxiliary Sensor Package (ASP) is a standalone payload inside the spacecraft bus which can be operated independently from the main Vector Sensor payload. The ASP provides contextual data to aid in the analysis of the science data from the Vector Sensor. A custom PCB (Hrafn) was designed and fabricated; this PCB includes both the implementation of the magnetic sensing system described in Chapter 7 and supporting electronics including a Raspberry Pi Zero as the payload computer. All ASP components are housed in an aluminum enclosure approximately 1/3 U in volume. The software residing on the Raspberry Pi implements a command and telemetry dictionary to abstract hardware complexity away into a simple interface for payload operation.